

Calmodulin–Calcineurin Interaction beyond the Calmodulin-Binding Region Contributes to Calcineurin Activation

Bin Sun,^{†,ID} Darin Vaughan,[†] Svetlana Tikunova,[§] Trevor P. Creamer,^{‡,ID} Jonathan P. Davis,[§] and P. M. Kekenes-Huskey^{*,||,⊥}

[†]Department of Chemistry, University of Kentucky, Lexington, Kentucky 40506, United States

[‡]Center for Structural Biology and Department of Molecular & Cellular Biochemistry, University of Kentucky, Lexington, Kentucky 40536, United States

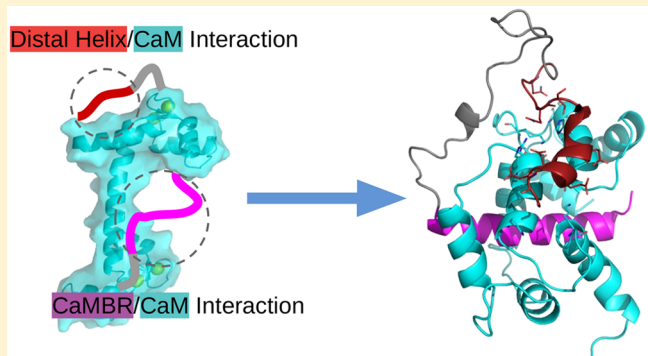
[§]Department of Physiology and Cell Biology, The Ohio State University, Columbus, Ohio 43210, United States

^{||}Department of Chemical and Materials Engineering, University of Kentucky, Lexington, Kentucky 40506, United States

[⊥]Department of Cell and Molecular Physiology, Loyola University Chicago, Maywood, Illinois 60153, United States

Supporting Information

ABSTRACT: Calcineurin (CaN) is a calcium-dependent phosphatase involved in numerous signaling pathways. Its activation is in part driven by the binding of calmodulin (CaM) to a CaM recognition region (CaMBR) within CaN's regulatory domain (RD). However, secondary interactions between CaM and the CaN RD may be necessary to fully activate CaN. Specifically, it is established that the CaN RD folds upon CaM binding and a region C-terminal to CaMBR, the “distal helix”, assumes an α -helix fold and contributes to activation [Dunlap, T. B., et al. (2013) *Biochemistry* 52, 8643–8651]. We hypothesized in that previous study that this distal helix can bind CaM in a region distinct from the canonical CaMBR. To test this hypothesis, we utilized molecular simulations, including replica-exchange molecular dynamics, protein–protein docking, and computational mutagenesis, to determine potential distal helix-binding sites on CaM's surface. We isolated a potential binding site on CaM (site D) that facilitates moderate-affinity interprotein interactions and predicted that mutation of site D residues K30 and G40 on CaM would weaken CaN distal helix binding. We experimentally confirmed that two variants (K30E and G40D) indicate weaker binding of a phosphate substrate *p*-nitrophenyl phosphate to the CaN catalytic site by a phosphatase assay. This weakened substrate affinity is consistent with competitive binding of the CaN autoinhibition domain to the catalytic site, which we suggest is due to the weakened distal helix–CaM interactions. This study therefore suggests a novel mechanism for CaM regulation of CaN that may extend to other CaM targets.



Downloaded via LOYOLA UNIV CHICAGO on April 7, 2020 at 15:58:54 (UTC).
See https://pubs.acs.org/sharingguidelines for options on how to legitimately share published articles.

raphy^{4–9} and nuclear magnetic resonance spectroscopy.¹⁰ Among the many CaN structures that have been deposited in the Protein Data Bank (PDB) are examples that have revealed the phosphatase's autoinhibited state (PDB entry 1au1⁴), a 2:2 CaM/CaN stoichiometric configuration,^{7,11,12} complexes of the enzyme with immunosuppressants,^{5,8} and transcription factors.^{6,9} However, much less is known about the structural basis of CaM-dependent regulation of CaN, as atomic-resolution CaM–CaN complexes are limited to intact CaM bound to small peptides comprising the CaMBR of the CaN regulatory domain.¹³ From those structures, while it is clear that the CaMBR assumes an α -helical secondary structure when bound to CaM, the paucity of structural information

Calcineurin (CaN) is a phosphatase that contributes to gene expression in response to changes in Ca^{2+} homeostasis. It plays integral roles in neurological development and maintenance, immune responses, and tissue remodeling.^{2,3} CaN is a heterodimeric protein consisting of two domains. Chain A (57–61 kDa) contains the protein's catalytic site, while chain B (19 kDa) contributes to enzyme regulation.³ CaN is activated by increasing intracellular Ca^{2+} levels. While it presents modest catalytic activity in response to Ca^{2+} alone, optimal phosphatase activity occurs upon binding of Ca^{2+} -saturated calmodulin (CaM) to the CaN regulatory domain. At decreased Ca^{2+} levels, the enzyme is inhibited by its autoinhibitory domain (AID) that directly binds to the phosphatase's catalytic site.

Our current understanding of the phosphatase's activation and enzymatic activity has been shaped by a number of atomic-resolution structures of CaN determined by X-ray crystallog-

Received: July 22, 2019

Revised: August 23, 2019

Published: September 4, 2019

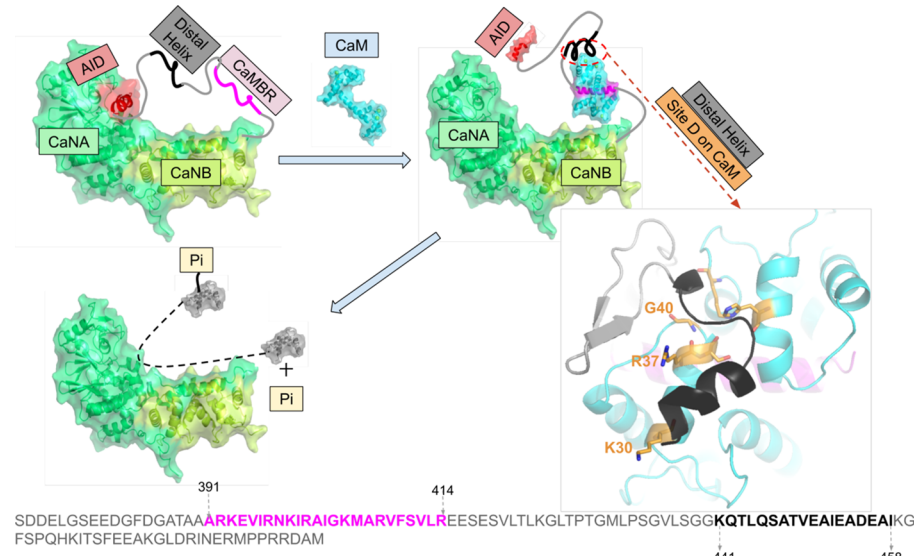


Figure 1. Refined model of activation of calcineurin (CaN) by calmodulin (CaM) through direct binding of the “distal helix” to CaM, based on the mechanism initially proposed in ref 1. The two chains of CaN (CaNA and CaNB) are colored green and lime green, respectively. AID is colored red. CaM is colored cyan. CaMBR is colored magenta. The amino acid sequence of CaN RD is shown at the bottom of the panel with CaMBR and the distal helix region colored magenta and black, respectively. In the absence of CaM, CaN is inhibited by its autoinhibitory domain (AID). After CaM binds the CaM-binding region (CaMBR) in CaN’s regulatory domain, a secondary interaction between CaM and a “distal helix” ultimately removes the AID from the CaN catalytic site. The activated CaN catalyzes the dephosphorylation of target proteins essential to myriad physiological functions.

inclusive of complete CaM and CaN proteins leaves critical details of CaM-dependent CaN regulation unresolved.

It is increasingly understood that CaM-dependent CaN activation depends on the structural properties of the 95-residue (≈ 10 kDa) CaN regulatory domain.¹⁴ This segment is intrinsically disordered,^{4,13–15} which signifies that it does not assume a well-defined fold in solution. Probes of its conformational properties in the absence and presence of Ca^{2+} -activated CaM have revealed important clues about the mechanism of CaN regulation. It was first observed via circular dichroism (CD) by Rumi-Masante et al.¹⁴ that upon CaM binding, nearly 50 residues of the RD folded into α -helices, of which the CaMBR region could account for only half. By using hydrogen/deuterium exchange mass spectrometry (HXMS), they further identified a region C-terminal to the CaMBR that formed an α -helix upon CaM binding.¹⁴ Dunlap et al.¹ confirmed the observation in a mutagenesis study of that region. Namely, they revealed that single-point mutations of three alanines within the distal helix region (DH, residues K441–I458) into glutamic acids disrupted helix formation. Importantly, these mutations decreased CaN’s apparent affinity for a substrate, *p*-nitrophenyl phosphate (pNPP), that competes with the AID for the CaN catalytic site.¹

Simulations of CaN have helped bridge experimental probes of its phosphatase activity^{3,16,17} with static, atomistic-resolution structural data. Li et al. reported conformational changes of the CaN B domain following Ca^{2+} binding via molecular dynamics (MD) simulation and proposed that the similarity of the apo-to holo-CaN B-domain conformations enables the former to regulate CaN activity independent of Ca^{2+} .¹⁸ Harish et al. utilized virtual screening and MD simulations to design inhibitory peptides of CaN using the native AID peptide as a template.¹⁹ Simulations have also been used to study the involvement of CaN residues outside of its catalytic domain in the binding and anchoring of inhibitory immunosuppressant drugs and analogues thereof.^{20–23} Similarly, computational

studies examining structural mechanisms of CaM-dependent regulation of targets have emerged recently, including myelin basic protein (MBP)²⁴ and myosin light chain kinase (MLCK).^{25,26} As a complement to these studies, we have additionally shown via MD and Brownian dynamics simulations that the CaMBR is highly dynamic in solution in the absence of CaM, that CaM binding to the CaMBR is diffusion-limited, and that the corresponding association rates are tuned by the charge density of the CaN peptide.²⁷ Despite these contributions, the sequence of molecular events that follow CaMBR binding and culminate in the relief of CaN autoinhibition remains unresolved.

Observations in refs 1, 14, and 28 formed the basis of a working model of CaN activation whereby the folding of the intrinsically disordered distal helix into an α -helix-rich structure is coupled to the relief of CaN autoinhibition. However, it was still unclear whether the distal helix directly binds to CaM and, if so, where they might share protein-protein interaction (PPI) interfaces or how those putative PPIs are stabilized. In large part, the challenge in identifying potential PPI sites arises because such interaction sites generally assume large, flat surfaces lacking specific interaction patterns,²⁹ such as grooves formed between α -helical bundles.^{30,31} Computational protein–protein docking engines have begun to address this challenge, including ZDOCK³² and RosettaDOCK³³, which have been used to successfully elucidate structural details of intrinsically disordered peptide-dependent regulation. For example, Hu et al. utilized ZDOCK to successfully predict the modes of binding between the disordered *Yersinia* effector protein and its chaperone partner.³⁴ Schiffer et al. explored the molecular mechanism of ubiquitin transfer starting from the top-ranked ZDOCK-predicted binding pose between ankyrin repeat and SOCS box protein 9 (ASB9) and creatine kinase (CK).³⁵ Bui et al. reported that phosphorylation of the intrinsically disordered fragment of transcription factor Ets1 leads to more binding of

competent structures to its coactivator as evidenced by MD and RosettaDOCK.³⁶ Our studies have therefore used vetted protein–protein docking techniques and extensive MD to uncover and validate plausible sites for the secondary interaction between CaN’s distal helix motif and CaM.

In this study, we combined a molecular model of CaM-dependent CaN activation with an expression to approximate its phosphatase activity. This entailed using computational methods, including protein–protein docking, enhanced sampling, and classical MD simulations, to identify potential sites of interaction between the distal helix and CaM. The protein–protein docking yielded several candidate interaction sites that we defined as sites A–D. Of these, site D on the CaM solvent-accessible surface appears to stabilize the distal helix by moderate-affinity intermolecular interactions. Among the intermolecular interactions stabilizing this putative PPI are two residues, lysine (K30) and glycine (G40), found on the “backside” of CaM distal to where CaMBR is known to bind. K30E and G40D mutations were found to abolish enzyme activity³⁷ in another globular CaM target, myosin light chain kinase (MLCK), that apparently relies on still unresolved secondary interactions to initiate catalysis.^{38,39} Analogously, our simulations of CaM K30E and G40D variants indicate that the mutations substantially impair distal helix binding at site D. As a complement to these simulations, we demonstrate that the distal helix A454E variant also destabilizes the distal helix–site D interaction in agreement with the decreased phosphatase activity shown by Dunlap et al.¹ Our data strongly suggest that the site D and CaN distal helix region are important to CaN activation, as we confirmed via experiment that the site-directed variants at site D residues K30 and G40 slow CaN-dependent dephosphorylation of pNPP. On the basis of these results, we provide an updated structural model of CaN activation by CaM that reflects specific CaM–distal helix interaction sites (see Figure 1) beyond the classical CaM-peptide-binding motif. We qualitatively rationalize that this mechanism controls the effective concentration of the AID near CaN’s catalytic site and, by extension, CaN’s catalytic activity.

METHODS

Our simulation protocol consisted of four primary steps: (1) replica-exchange molecular dynamics (REMD) simulations to generate trial conformations of the isolated CaN distal helix region, (2) ZDOCK protein–protein docking to yield initial poses for putative CaM–CaN interaction sites, (3) refinement of poses using extensive, microsecond-length molecular dynamics simulations, and (4) molecular mechanics-generalized Born and surface area continuum solvation (MM-GBSA) to rank-order distal helix–CaM pose interaction scores. We further challenged the predicted structural models by introducing mutations into the distal helix and putative interaction site D.

Replica-Exchange Molecular Dynamics (REMD) Sampling of the Isolated Distal Helix. In accordance with our approach in ref 27, we performed REMD simulations of the distal helix region (K441–I458) in the absence of CaM to exhaustively sample likely conformations that are in equilibrium. The distal helix peptide was constructed by the auxiliary TLEAP program in Amber16⁴⁰ in an extended configuration and parametrized using the Amber ff99SBildn⁴¹ force field. The peptide was then minimized via SANDER⁴² *in vacuo* until the energy gradient converged ($\text{drms} \leq 0.05$) or the number of

steps, 1×10^5 (with the first 50 steps being steepest descent and the rest of the steps being a conjugate gradient algorithm), was satisfied. The minimized structure was then used as the starting structure for REMD simulations coupled with the Hawkins, Cramer, Truhlar pairwise generalized Born implicit-solvent model⁴³ via the $igb = 1$ option in Amber. The monovalent 1:1 salt concentration was set to 0.15 M, and a nonbonded cutoff of 99 Å was chosen. Ten replicas were created with a temperature range of 270–453 K. The temperature of each replica was calculated via the Patriksson et al. Web server⁴⁴ to ensure the exchange probability between neighboring replicas was approximately 0.4, as recommended in refs 45 and 46. Each replica was first subjected to 1×10^5 steps of energy minimization via PMEMD with the first 50 steps via steepest descent and the remaining steps via conjugate gradients. The minimized systems were subsequently heated from 0 K to their respective target temperatures over an 800 ps interval using a time step of 2 fs with a Langevin thermostat. The equilibrated replicas were then subjected to 100 ns production REMD simulations under the target temperature with a Langevin thermostat. The SHAKE⁴⁷ algorithms were also used for REMD simulations. Clustering analyses with a hierarchical agglomerative (bottom-up) approach using CPPTRAJ were conducted on the 300 K REMD trajectory to divide the trajectory into 10 clusters; the average root-mean-squared deviation (RMSD) between each cluster was approximately 6 Å.

Docking of the Distal Helix to the CaM–CaMBR Complex via ZDOCK. The protein–protein docking Web server ZDOCK 3.0.2³² was used to determine probable binding poses for the REMD-generated distal helix conformations on the CaMBR-bound CaM complex. The CaM–CaMBR complex configuration was obtained from the PDB (entry 4q5u²⁸). It has been reported that 62% of experimentally resolved PPIs are characterized by the binding of an α -helical peptide within grooves formed between adjacent α -helices on the target protein surface;³¹ therefore, we narrowed the ZDOCK search to four α -helix-containing regions on the CaM solvent-exposed surface. These sites are shown in Figure 2a, from which we determined a list of probable amino acid contacts as input to ZDOCK (see Table S1). During the ZDOCK calculations, the receptor (CaM–CaMBR complex) was kept fixed while grids were constructed around the receptor with dimensions of 80 Å × 80 Å × 80 Å and a spacing of 1.2 Å. The ligand (distal helix) was then docked via the fast Fourier transform (FFT) algorithm on the three-dimensional grids. The scoring function consists of interface atomic contact energies (IFACEs),⁴⁸ shape complementarity, and electrostatics with charge adopted from the CHARMM19 force field.⁴⁹ The 2×10^3 generated poses were subjected to a culling process to eliminate those having no contacts with residues we specified in Table S1. After culling, there were zero, two, 88, and three poses left at sites A–D, respectively. The pose with the highest score at each site was chosen for further refinement using molecular dynamics.

Conventional Molecular Dynamics (MD) Simulations of ZDOCK-Generated Distal Helix–CaM Poses. Explicit-solvent MD simulations were performed on the ZDOCK-predicted distal helix–CaM complexes to further refine the distal helix binding poses. The amino acid sequence from the CaMBR to the distal helix is shown at the bottom of Figure 1, and the sequence definition of CaMBR and distal helix is the same as that in ref 1. We first inserted peptide linkers for each

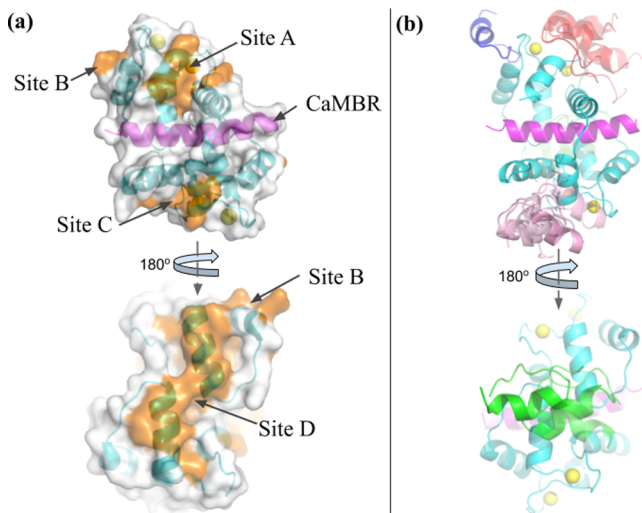


Figure 2. (a) Four tentative binding sites (orange) on the surface of the CaM–CaMBR complex. CaM is colored cyan. CaMBR is colored magenta. Ca²⁺ ions are colored yellow. (b) ZDOCK-predicted conformations of the distal helix interacting with the CaM–CaMBR complex at each site. Predicted distal helix conformations from site A to D are colored red, blue, pink, and green, respectively.

pose between the CaMBR C-terminus (R414) and the N-terminus (K441) of the distal helix via TLEAP. The initial linker was generated via TLEAP and energy-minimized as described in **Replica-Exchange Molecular Dynamics (REMD) Sampling of the Isolated Distal Helix**. The minimized structures were subsequently simulated *in vacuo* to heat the systems from 0 to 300 K. The last frame of the short equilibration run was subject to additional energy minimization *in vacuo* to facilitate its compliance with the distal helix and CaMBR terminus. The top poses from ZDOCK presented distal helix orientations that were all compatible with the CaMBR and linker configurations. The optimized linker was placed adjacent to the CaMBR and the distal helix; TLEAP was then used to link the peptide components. The resulting structures were then subjected to energy minimization, followed by a 100 ps heating process to increase the system temperature to 300 K, for which all atoms except the linker were fixed via the *i belly* function in the SANDER MD engine of Amber. This minimization and heating were performed *in vacuo* to further relax the linker in the presence of the distal helix and CaM–CaMBR complex. The last frame of the heating stage was used as an input configuration for explicit-solvent MD simulations.

Each *in vacuo* starting configuration was solvated in a TIP3P⁵⁰ water box with 12 Å boundary margin. K⁺ and Cl⁻ ions were added to neutralize the protein and establish a salt concentration of 0.15 M. After the system had been parametrized using the ff14SB force field⁵¹ via TLEAP, the system was subjected to energy minimization, for which all atoms except hydrogens, waters, and KCl ions were constrained by the *i belly* function. The cutoff value for nonbonded interactions was set to 10 Å. A 2 fs time step was chosen, as SHAKE⁴⁷ constraints were applied on bonds involving hydrogen atoms. Two heating procedures were performed to heat the system from 0 to 300 K using the Amber16 SANDER.MPI engine.⁴² In the first heating stage, the *i belly* function was used to keep the protein fixed and the surrounding solvent unrestrained. The water box was heated to 300 K over a 100 ps interval under the NVT ensemble. For the second heating

stage, the entire system was heated from 0 to 300 K over 500 ps under the NPT ensemble, for which the backbone atoms of CaM, CaMBR, and the distal helix were constrained by a harmonic potential (force constants of 3 kcal mol⁻¹ Å⁻²). Thereafter, an additional 1 ns equilibrium stage was conducted at 300 K under the same constraints but with a reduced force constant of 1 kcal mol⁻¹ Å⁻². These equilibrium simulations were followed by 100 ns production-level MD simulations. The weak-coupling thermostat⁵² was used during the simulation. Clustering analysis was performed on the production trajectory using the same strategy described in **Replica-Exchange Molecular Dynamics (REMD) Sampling of the Isolated Distal Helix**. The average RMSD between each cluster was approximately 6 Å. On the basis of the rationale that extending simulations using less frequently sampled structures provides greater overall sampling of the conformational space,⁵³ we identified five or six low-probability states as inputs for subsequent MD simulations. Approximately 1 μs of trajectory data was simulated in total for each site.

MD Simulations of CaM (K30E and G40D) and the CaN Distal Helix Variant (A454E).

Clustering analyses were performed on the production-level MD trajectories of the distal helix–CaM configurations that yielded the most favorable binding scores by MM-GBSA. The binding free energy between the distal helix and CaM was estimated via MM-GBSA^{54,55} as follows

$$\Delta G = \langle G_{DH-CaM} \rangle - \langle G_{CaM} \rangle - \langle G_{DH} \rangle \quad (1)$$

where $\langle G_{DH-CaM} \rangle$, $\langle G_{CaM} \rangle$, and $\langle G_{DH} \rangle$ are ensemble-averaged free energies of the distal helix–CaM complex, CaM, and the distal helix, respectively. A representative structure of the most populated cluster was selected as input for *in silico* mutagenesis to validate the model against experiment. Namely, the CaM K30E and G40D variants, as well as the CaN A454E variant, were built by replacing and regenerating the amino acid side chains using TLEAP. Because the predicted A454E distal helix poses appeared to be inferior to those of the wild-type (WT) variant, we refined only the WT poses and thereafter introduced A454E mutations into the refined conformations. The resulting structures were energy minimized with a stop criterion of ($drms \leq 0.05$) for the energy, during which all atoms except the mutated residues were fixed via the *i belly* function in Amber. The energy-minimized structure was then solvated and simulated according to the same procedure described in **Conventional Molecular Dynamics (MD) Simulations of ZDOCK-Generated Distal Helix–CaM Poses**. All simulation cases in this study are listed in Table S3. In the MM-GBSA calculations, the trajectories of these three components in eq 2 were extracted from MD trajectories via CPPTRAJ at a 2 ns frequency. The generated subtrajectories were used as input of MMPBSA.py in Amber16 to calculate the free energies of each part. The salt concentration was set as 0.15 M with the generalized Born model option setting as *igb* = 5. No quasi-harmonic entropy approximation was made during the calculation.

Structural Analyses. Clustering analysis, root-mean-square deviation (RMSD)/root-mean-square fluctuation (RMSF) calculations, hydrogen bond analysis, and secondary structure analysis were performed via CPPTRAJ⁵⁶ in Amber16. The reference structure used for these analyses was the CaM–CaMBR crystal structure (PDB entry 4q5u²⁸). The secondary structure for each residue was calculated using CPPTRAJ with the Define Secondary Structure of Proteins (DSSP) algorithm.⁵⁷

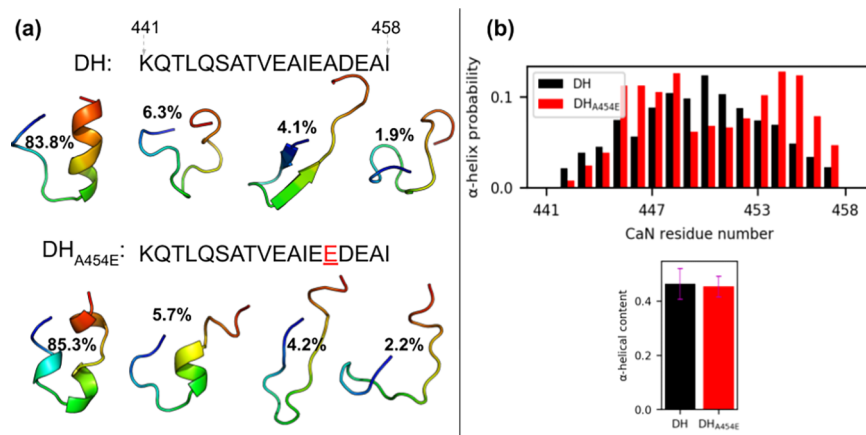


Figure 3. (a) Sequences of the distal helix and DH_{A454E} and representative structures of the four most populated clusters from 100 ns REMD simulations. The structures are colored in rainbow with the N-termini colored blue and the C-termini colored red. (b) Secondary structure probability of each residue calculated from the REMD trajectory via CPPTRAJ with the DSSP algorithm. The bottom panel shows the total α -helix content of the two fragments calculated via the COLVAR module of VMD.

The COLVAR module⁵⁸ within VMD was used to assess the total α -helix content of the REMD-generated distal helix and DH_{A454E} conformation. The *hbond* command within CPPTRAJ was used to analyze hydrogen bonds between distal helix and the CaM–CaMBR complex. During the *hbond* analysis, the angle cutoff for hydrogen bonds was disabled while the default 3 Å cutoff between acceptor and donor heavy atoms was used. Scripts and CPPTRAJ input files used for these analyses will be publicly available at <https://bitbucket.org/pkhlab/pkh-lab-analyses/src/default/2018-CaMDH>.

Calcineurin Phosphatase Assay Using the p-Nitrophenyl Phosphate (pNPP) Substrate. *Materials.* pNPP was obtained as the bis(tris) salt (Sigma). Dithiothreitol was the reducing agent (Sigma). Assay buffer consisted of 80 mM Tris (pH 8), 200 mM KCl, and 2 mM CaCl₂, and 50 mM MnCl₂ was used as a CaN activating cofactor.

Preparation of Enzymes and Proteins. The CaM WT, K30E, and G40D variants were generated, expressed, and purified as previously described.³⁷ CaN was expressed from the pETTagHisCN plasmid (from Addgene, Cambridge, MA) in *Escherichia coli* BL21 (DE3) CodonPlus RIL cells (Agilent, La Jolla, CA). The enzyme was unified via a Ni-NTA column followed by a CaM-sepharose column (GE Healthcare, Piscataway, NJ) as described in ref 14.

Enzyme Assay. Phosphatase assays were performed using 30 nM CaN and 90 nM CaM in 96-well Corning Costar microtiter plates with a reaction volume of 120 μ L. Assays proceeded in the manner described in ref 1 with each CaM assayed in triplicate and over three plates to account for technical variation. Control reactions without CaN were added to the end of each lane with 200 mM pNPP to determine the rate of enzyme-independent substrate hydrolysis.

Kinetic Analysis. The pNPP substrate reactions were varied over 11 concentrations, increasing from 0 to 200 mM for each column; 60 min absorbance readings were obtained on a Molecular Devices FlexStation 3 plate reader using Softmax Pro 7 software at 405 nm with 10 min read intervals. The resulting data were inspected for appropriate Michaelis–Menten kinetics by plotting the initial velocity (V) against substrate concentration. Readings were linearized to produce the double-reciprocal Lineweaver–Burk plot for estimation of V_{max} and K_M based on the equation

$$\frac{1}{V} = \frac{K_M}{V_{\text{max}}} [\text{pNPP}] + \frac{1}{V_{\text{max}}} \quad (2)$$

RESULTS

Prior studies^{14,59} have indicated that binding of CaM to CaN's canonical CaM-binding region requires secondary interactions beyond that region to fully activate the phosphatase. A study by Dunlap et al.¹ suggested that a distal helix region spanning residues K441–I458 engages in a secondary interaction that is likely involved in CaM binding. However, it was unclear which region(s) of the CaM solvent-exposed surface would contribute to a potential PPI. We therefore used MD and protein–protein docking simulations to identify plausible WT CaN interaction sites on CaM and challenge these predictions with mutagenesis. Our predicted site was validated using a CaN pNPP phosphatase assay.

Regulatory Domain (RD) Construct Propensity for Secondary Structure Formation in the Absence of CaM. Circular dichroism (CD) and HXMS analysis in ref 14 suggest that an α -helical structure exists beyond the canonical CaMBR region after CaM's binding. We therefore sought to assess α -helicity in the REMD-simulated distal helix peptides. Previously,²⁷ we found that extensive MD simulations of the isolated CaMBR yielded a small population of α -helical structures suitable for binding CaM in its canonical binding pose.⁶⁰ We therefore applied a similar REMD procedure (see **Replica-Exchange Molecular Dynamics (REMD) Sampling of the Isolated Distal Helix**) to the proposed distal helix segment of the CaN regulatory domain to assess the propensity for the spontaneous formation of secondary structure in the absence of CaM. Here, we performed 100 ns REMD simulations on the WT distal helix as well as an A454E variant. The latter was considered as it has been reported to exhibit reduced α -helical content in the presence of CaM,¹ which is suggestive of abolishing the distal helix–CaM interaction. Following the REMD simulations, we performed clustering analysis to identify the predominant conformations of the two peptide configurations. Interestingly, we observed that both the WT distal helix and its A454E mutant partially fold into an α -helix in the absence of CaM. As shown in Figure 3a, representative structures of the most populated clusters of the distal helix and A454E mutant (83.8% and 85.3% of the total trajectory,

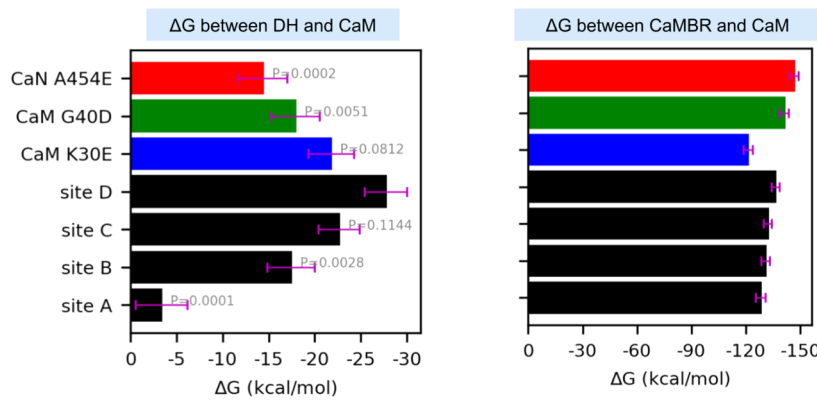


Figure 4. Approximate binding free energies between CaM and the distal helix (left) or CaMBR regions (right) determined via molecular mechanics generalized Born and surface area continuum solvation (MM-GBSA). Black bars correspond to wild-type CaN, whereas colored bars are for the A454E CaN and CaM variants. The calculation was conducted on frames extracted every 2 ns from MD trajectories. The error bars represent the standard error of the mean. The values above bars in the left panel are *p* values of each case with the null hypothesis that their mean values are equal to that of site D.

respectively) both contain helical fragments. While the overall α -helix contents ($\approx 45\%$) of these two fragments were statistically indistinguishable, a contiguous helix was formed in the WT distal helix, whereas it was fragmented in the mutant at the location of the A454E substitution. Our calculations indicate approximately five amide hydrogen bonds present in the WT distal helix (Figure S11), which maintain its moderate helical content. We note that experimental assays of the complete regulatory domain (RD) do not detect significant secondary structure; this discrepancy may be a result of using substantially different RD lengths (S374–Q522 in ref 14 versus K441–I458 in this study). We discuss this difference in further detail in Limitations.

Protein–Protein Interactions between the Regulatory Domain (RD) Construct and Peptide-Bound CaM. The overwhelming majority of CaM-containing complex structures resolved to date includes only limited fragments of the bound target protein.⁶⁰ CaM-bound CaN is no exception, as the mostly likely physiological conformation²⁸ consists of a monomeric CaM in a canonical “wrapped” conformation about a target region in CaN (A391–R414);¹³ however, it is evident that secondary interactions beyond this domain play a role in CaN activity, yet atomistic-level structural details of these interactions have not yet been resolved. Therefore, to resolve potential binding regions for the distal helix region, we seeded a protein–protein docking engine, ZDOCK,³² with candidate α -helical structures identified through REMD simulations. The docking simulations were performed in regions that included grooves formed between α -helices we identified at the CaM solvent-accessible surface. We selected these regions, because such secondary structures are believed to nucleate protein–protein interactions.⁶² Furthermore, a thorough examination of protein–protein complex structures in the PDB in 2011 suggested that α -helices contribute to 62% of all PPI interaction surfaces³¹ between binding partners. Narrowing the search region on CaM to those containing α -helical regions yielded four candidate sites (A–D) that spanned nearly the entire CaM solvent-exposed surface (see Figure 2a).

The most energetically favorable distal helix–CaM poses predicted via ZDOCK at sites A–D are summarized in Figure S1. The docked poses reflect significant interactions of at least the distal helix C-terminal loop with loops bridging adjacent α -helices on the CaM surface. At site A, polar residues near N97,

Y99, and D133 from two of the C-terminal CaM domain’s loops interact with the distal helix, compared with just one EF-hand motif loop at site B (D129, D133, and D135). The site C poses were primarily stabilized by hydrophobic interactions formed from CaN residues L444/I458 and F16/L4 on CaM, in addition to a loop–loop interaction via CaM D64. The site D poses reflected distal helix C-terminal loop interactions with CaM EF-hand loop residues near N42 and K94. Most poses were unsurprisingly parallel to α -helical/ α -helical “grooves” on the CaM solvent-exposed surface and were evidently anchored through interactions between the proteins’ loop regions.

In contrast, we found that the A454E variant docked poorly at sites A–D (see Figure S2), as assessed by the proximity of docked poses to the designated CaM sites. In fact, most predicted poses tended to localize toward site A, albeit with weak interactions. Moreover, we speculate that the impaired binding of DH_{A454E} may arise from its fragmented α -helical structure, in contrast to the contiguous regions for the WT variant (see Table S2 for docking scores and Figures S1 and S2 for docking poses). Although docking scores were provided by the ZDOCK algorithm to rank-order potential poses, we did not analyze these scores in detail as we later refined these structures using more detailed simulations and energy expressions. This refinement corrects for artifacts from the ZDOCK algorithm, which assumes rigid conformations for both proteins that would ordinarily be expected to relax in the bound complex. Hence, in the following section, we pursue extensive microsecond-scale all-atom MD simulations to refine and assess the predicted poses.

The docked CaN–CaM configurations from the previous section were intended as inputs for MD-based refinement of nearly intact CaN regulatory domain complexes with CaM. Subsequent refinement using microsecond-length MD simulations was used to relax the rigid protein conformations assumed in ZDOCK. We first assess the integrity of the predicted binding modes based on molecular mechanics generalized Born and surface area continuum solvation (MM-GBSA). MM-GBSA scoring of the MD-generated configurations provides a coarse estimate of binding affinity without significantly more expensive free energy methods. We reported the binding free energy of the distal helix between CaM as well as between the CaMBR and CaM in Figure 4. Significantly, we found that binding of the WT distal helix at

CaM site D yielded a more pronounced favorable average binding free energy ($\Delta G = -27.7 \pm 2.3 \text{ kcal mol}^{-1}$) compared to those of sites A–C (-3.3 ± 2.8 , -17.4 ± 2.6 , and $-22.6 \pm 2.2 \text{ kcal mol}^{-1}$, respectively) with p values (1×10^{-4} , 2.8×10^{-3} , and 1.144×10^{-1} , respectively) confirming that the means are significant compared to the null hypothesis. Notably, these thermodynamically favorable scores are also suggestive of the potential for the distal helix to bind multiple regions on the CaM surface, although site D is the most favorable site. Additionally, the binding free energies of distal helix interactions were generally substantially weaker (-3.3 to $-27.7 \text{ kcal mol}^{-1}$) than those between the CaMBR and CaM ($\Delta G < -120 \times 10^2 \text{ kcal mol}^{-1}$).

We supplement the energy scores with structural indicators of stability, namely, contacts and RMSF. We report in Figure 5

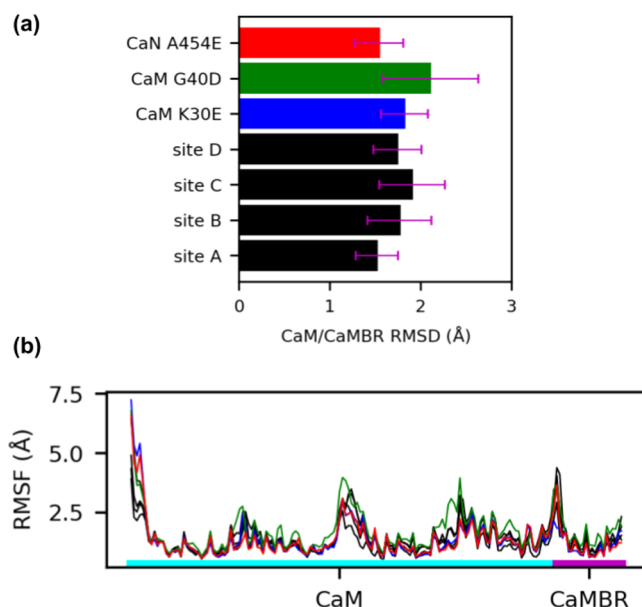


Figure 5. (a) Root-mean-square deviations (RMSDs) of the peptide backbone atoms of CaM and CaMBR from microsecond-length MD simulations. The reference structure for the RMSD calculation was the CaM–CaMBR crystal structure (PDB entry 4q5u). (b) Root-mean-square fluctuations (RMSFs) of non-hydrogen atoms in CaM and CaMBR.

the corresponding RMSDs and RMSFs of the peptide backbone atoms from CaM and the CaN CaMBR. We additionally include two CaM variants with mutations at site D to challenge our predicted pose. We found that the average RMSD values of the MD-predicted conformations relative to the experimentally determined CaM–CaMBR structure were $\leq 2 \text{ Å}$; we attribute these small fluctuations to stable CaM–CaMBR interactions that were insensitive to the distal helix docking. Similar to the RMSD data, the CaM and CaMBR RMSF values are comparable in amplitude and nearly indistinguishable between distal helix docking poses, with most residues presenting values of $< 1.5 \text{ Å}$. The prominent peaks in excess of 5.0 Å correspond to the CaM terminus and the N-terminus of the CaMBR. We additionally observe a variable region midway along the CaM sequence, which corresponds to the labile linker between its globular N- and C-terminal domains that is implicated in allosteric signaling.⁶³

The small and statistically indistinguishable RMSF values for the CaM–CaMBR complex in Figure 5 suggest that distal helix

binding had a negligible impact on binding of the CaM recognition motif. This is an important observation, as viable binding poses for the distal helix are expected to preserve the binding between the CaMBR and CaM. We base this assumption on CD data collected in ref 64 that indicated substantial α -helical character in the CaM–CaN complex following dissociation of the distal helix domain. In Figure 6, we report representative configurations of the distal helix region (red) in complex with CaM (cyan), as well as their corresponding per-residue RMSF values in Figure 7. To guide interpretation, we hypothesized that RMSF values of $> 5 \text{ Å}$ were indicative of poorly stabilized residues. At site A, both the distal helix–CaMBR linker and the distal helix reflect RMSF values in excess of ~ 10 and $\sim 15 \text{ Å}$, respectively. These large fluctuations arise from the breadth of binding orientations evident in Figure 6a, which we interpreted as poorly stabilized configurations. Similarly, the site B configurations also appeared to be loosely bound, based on linker and distal helix RMSF values beyond 10 Å . In contrast, the distal helix RMSF values at sites C and D were $< 5 \text{ Å}$, with the latter site reporting the smallest values among the sites we considered, which is indicative of a stable binding configuration.

As has been shown in other proteins regulated by disordered protein domains,^{65–67} there are often multiple poses that contribute to regulation. We therefore assessed the most significant interprotein contacts contributing to the ensemble of distal helix binding poses at sites A–D. Among these poses, the distal helix configurations at site D presented the lowest distal helix RMSF values among the considered sites. Significantly, the site D distal helix configuration exhibited several hydrogen bond-facilitated interactions with CaM, including two long-duration (37% and 55% of sampled configurations) interactions between Q445 and CaM residues R37/K94, pairing of CaM K21 with glutamic acids E453 and E450, and pairing of E456 with CaM residues K30 and R37. Contacts between CaM and CaN, as well as their duration (as assessed by the percentage of MD frames satisfying a hydrogen bond contact cutoff of 3 Å between oxygen and nitrogen atoms), are additionally quantified in Figure S4 (specific values listed in Table S4). The latter data indicate a modestly greater degree of hydrogen bonding of the distal helix at site D (10 H-bonds were above 10%) versus site B (9) and a significantly greater degree relative to sites A (1) and C (3). Furthermore, the site D pose appears to be stabilized by both the N- and C-terminal domains of CaM (residues D20–S38 and R90–N111, respectively). We speculate that this bidentate interaction could improve CaMBR binding by locking CaM into its collapsed configuration and thereby preventing disassembly. Although during the simulation the distal helix at site D maintained significant α -helical content (see Figures S3 and S5), we note that some of the predicted structures exhibited β -sheet character in the linker region (see Figure S6) that was not observed in the CD spectra collected by Rumi-Mansante et al.¹⁴ This persistent secondary structure was limited to a few residues (see Figures S6 and S7) and thus may have been beyond the limits of detection in earlier CD experiments. We comment on this further in Limitations. Meanwhile, site B reflected interactions with both CaM terminal domains that were attenuated relative to site D, while sites A and C were mostly bound by interactions of their linker regions with the CaM N-terminal domain. Interestingly, we observed that the distal helix poses originating at site B migrated toward site D

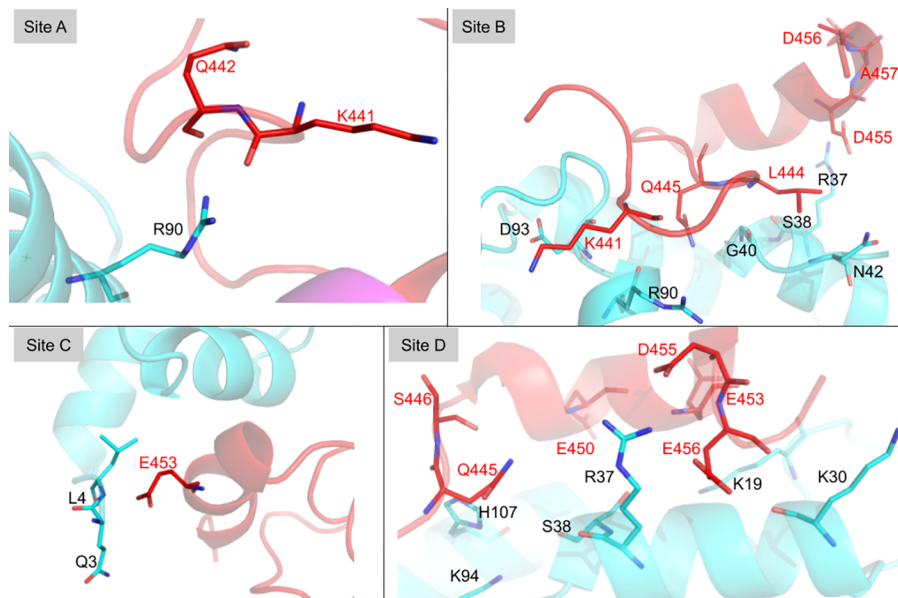


Figure 6. Interaction between the linker and distal helix of CaN and CaM at sites A–D. Key residues at the interaction surface are shown as sticks with black labels for CaM residues and red labels for distal helix residues. See Table S4 for the duration of these interactions.

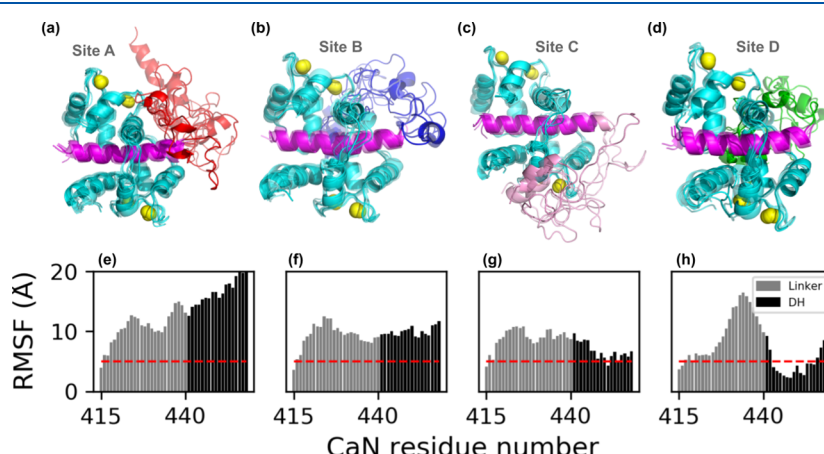


Figure 7. (a–d) Representative structures of the distal helix–CaM complex from microsecond-length MD simulations initialized from ZDOCK-predicted distal helix poses. CaM is colored cyan. CaMBR is colored magenta. Ca^{2+} ions are depicted as yellow spheres. The linker and distal helix regions in sites A–D are colored red, blue, pink, and green, respectively. (e–h) Non-hydrogen atom RMSFs of the linker and distal helix residue calculated from MD simulations of each site, as an indicator of binding stability. The red dashed lines depict RMSF values of 5 Å. During the MD simulations, distal helix structures initiated at site B migrated toward site D (Figure S3).

(see Figure S3), which likely explains the higher level of hydrogen bonding in site B versus sites A and C.

As a result of HXMS conducted by Rumi-Masante et al.¹⁴ of the RD construct of CaN in solution with CaM, it is apparent that residues R414–E456 are within a stretch of residues that are somewhat protected from solvent, which suggests that relief of CaN autoinhibition entails binding at least the distal helix region. We note that the HXMS data could not precisely distinguish which residues were protected, as proteolysis and mass spectrometry were conducted on short peptides. In addition, HXMS data detect only bonds involving backbone amide protons; thus, we speculate that the CaN side chain interactions with CaM may stabilize the distal helix α -helical structure. Hence, we suggest that CaM–CaN configurations that stabilize the distal helix region likely contribute to CaN activation. On the basis of this rationale, the small RMSF values and extensive hydrogen bonding of the CaN distal helix

with CaM site D relative to other ZDOCK-identified regions suggest that CaN is most stabilized at site D.

Effects of Distal Helix–CaM Site D Mutagenesis. MD simulations of the WT CaN CaMBR–distal helix sequence suggest that CaM site D is a probable binding region for the CaN regulatory domain. To challenge this hypothesis, we performed MD simulations of CaN distal helix and CaM site D variants to test whether the distal helix–CaM interaction was impaired. Namely, we introduced the CaN A454E as well as CaM K30E and G40D mutations into the MD-optimized WT structures in accordance with prior experimental studies of CaN¹ and the MLCK.³⁷ We elected to mutate the WT CaMBR–distal helix complexes with CaM, as the WT complex appeared to have favorable stability, whereas repeating the REMD/ZDOCK steps with the mutants may not have yielded viable configurations. The proposed A454E CaN variant was based on CD data collected by Dunlap et al.¹ that demonstrated reduced α -helical content upon binding CaM

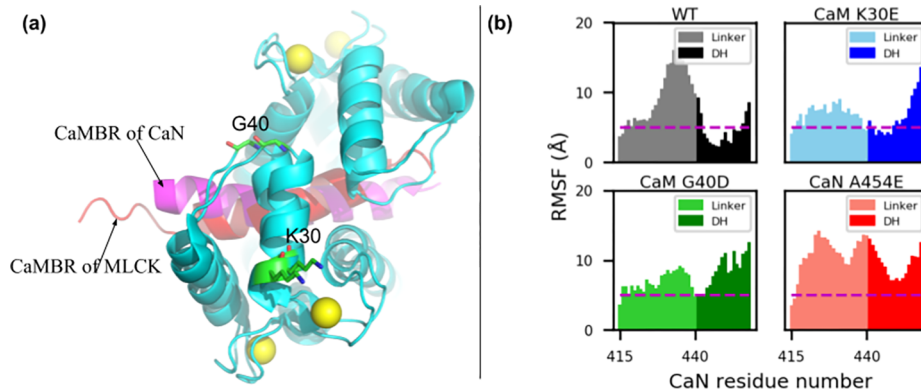


Figure 8. (a) Comparison of the CaM–peptide complex structure from CaN and MLCK (PDB entry 2lv6⁶⁸). K30 and G40 are labeled (shown as sticks) on the basis of their implication in the activation of the CaM target MLCK³⁷ and proximity to site D determined by our simulations. (b) Non-hydrogen RMSFs of the linker and distal helix in the WT and mutants. The dashed lines depict RMSFs of 5 Å. The hydrogen bonds formed between the distal helix and CaM of these variants are shown in Figure S9.

relative to the WT with impaired CaN activation. The CaM variants we examined in this study were based on studies³⁷ of the CaM-dependent MLCK activation, for which secondary interactions beyond the canonical CaM-binding motif were implicated in enzyme activation^{38,39} (Figure 8a). Although these secondary CaM interactions are involved in directly binding the MLCK catalytic domain in contrast to CaN,³⁸ two residues (K30 and G40) implicated in binding³⁷ reside within the site D identified in our simulations.

We reported MM-GBSA-calculated binding free energies between the distal helix and CaM of the mutants from MD simulations of these variants in Figure 4. While the WT distal helix at CaM site D had the most stable binding with a ΔG of -27.7 ± 2.3 kcal mol⁻¹, the K30E, G40D, and A454E mutations had less favorable ΔG values of -21.8 ± 2.5 , -17.9 ± 2.6 , and -14.4 ± 2.6 kcal mol⁻¹, respectively (p values of 8.12×10^{-2} , 5.1×10^{-3} , and 2×10^{-4} , respectively). The MM-GBSA energies suggest that mutations would impair binding between the distal helix and CaM. Accordingly, we present the linker and distal helix RMSF data for the WT and mutants in Figure 8b. The distal helix RMSF values for the two CaM variants were moderately increased compared to those of the WT. Specifically, for the WT system, the distal helix residues were entirely within 10 Å and as low as ~2.5 Å. In contrast, the K30E variant yielded RMSF values no smaller than approximately 5 Å, while the C-terminal half approaches values nearing 15 Å. This trend manifested in fewer long-lived hydrogen bond contacts between the distal helix and both CaM domains (see Figure 8). Similarly, the G40D mutation appeared to significantly disrupt interactions with CaN, as the entire distal helix region was characterized with RMSF values of $\gtrsim 10$ Å, with corresponding decreases in the number of hydrogen bond contacts. Among the mutants we considered, the A454E mutant had the most severe impact on RMSF values, as all residues comprising the linker and distal helix regions resulted in fluctuations of > 8 Å. We also reported the α -helix probability of distal helix residues for variants in Figure S8. It was found that all variants preserved a significant degree of overall helicity despite evidence of impaired interactions with CaM. However, the specific residues that formed the α -helix were different among the variants. The mutation of A454 to E454 shifted the helicity to the first half of the distal helix, while the two CaM variants reflected α -helices in the C-terminal region. Altogether, these simulation data suggest that (1) the

WT distal helix is stabilized at the site D CaM region, (2) site D residues K30 and G40D are implicated in distal helix binding, and (3) disruption of site D binding by CaN A454E is consistent with reduced helicity and enzyme activity measured experimentally.

Phosphatase Assays of Site-Directed CaM Mutants.

To validate the simulation results, namely that CaM site D stabilizes the distal helix and thereby promotes CaN activity, we analyzed the kinetics of CaN-mediated hydrolysis of pNPP. We hypothesized that disruption of site D–distal helix binding would decrease the accessibility of the catalytic site for pNPP binding by allowing the AID to bind to a greater extent. This could manifest as a reduced apparent substrate affinity. We therefore conducted CaN phosphatase assays with a pNPP substrate using two site D variants, K30E and G40D. We analyzed substrate turnover in a Michaelis–Menten model, as described in Methods. Phosphatase assays performed on CaM variants strongly suggest a statistically significant reduction (p values in Table 1) in catalytic activity by a substantial increase

Table 1. Kinetic Parameters of pNPP Dephosphorylation with WT CaM and Two Site D Variants^a

CaM	K_M (mM)	standard deviation	p value
WT	27.6	1.3	—
K30E	46.0	2.8	0.002
G40D	35.5	2.2	0.008

^a p values determined by Welch's *t*-test for the difference of means with unequal variance.

in K_M for K30E and G40D (46.0 ± 2.8 and 35.5 ± 2.2 mM, respectively) versus that of the WT (27.6 ± 1.3 mM), indirectly indicating weaker binding of the distal helix peptide to the mutated CaM construct.

DISCUSSION

Summary of Key Findings. We have used computational modeling and experiment to elucidate a potential mechanism for CaM-dependent regulation of CaN activity, whereby the binding of a “distal helix” region of the regulatory domain relieves CaN autoinhibition. Our microsecond-duration MD simulations indicate that the distal helix region remains bound to the solvent-accessible CaM surface, which could weaken the ability of the AID to bind CaN’s catalytic site (see Figure 1). In

contrast, we predict that an engineered variant (A454E) disrupts the domain's secondary structure and ability to competently bind CaM. Both predictions are in agreement with experimental probes of CaN regulatory domain structure and phosphatase activity.¹ Namely, among the four potential regions on CaM's surface that were solvent-accessible after binding the CaMBR, our data suggest that a regulatory domain (RD) region spanning the CaMBR through the distal helix was best stabilized at a site nestled between the CaM N- and C-terminal domains. In silico mutagenesis of two N-terminal CaM residues (K30E and G40D) prevented distal helix binding in our model, which we suggest hinders CaN activation, similar to identical mutations in CaM that were found to inactivate another CaM target, MLCK. We confirmed the potential CaM site D binding site for the distal helix through site-directed K30E and G40D variants, which we found to weaken CaN binding as reflected by decreased (weakened) MM-GBSA scores and an increase in K_M (from 27.6 mM to 46.0 mM and 35.5 mM, respectively) in a pNPP phosphatase assay. Although our REMD simulations suggest that the isolated distal helix region spontaneously assumes moderate α -helical structure in the absence of CaM, in contrast to trends observed in the complete regulatory domain (RD) observed experimentally,¹⁴ we do not believe this significantly impacts our suggestion that site D contributes to CaN activation. We discuss this further in [Limitations](#).

Plausible Binding Modes for the CaN Distal Helix with CaM. Previous studies suggest that (1) binding of regulatory domain residues beyond the CaMBR is involved in CaM-dependent relief of CaN autoinhibition,^{1,14} based on increases in the regulatory α -helical content reported upon binding CaM that could not be accounted for by the CaMBR alone, (2) alanine to glutamic acid mutations at regulatory domain (RD) positions (A451E, A454E, and A457E) C-terminal to the CaMBR decrease the α -helical content and CaN activity, and (3) HXMS studies indicate reduced solvent accessibility for the distal helix relative to the entire regulatory domain (RD) for a complex formed between CaM and a CaN regulatory domain–AID–C-terminal domain construct (see [section S1.4](#) for further discussion). While we believe site D is the most probable site for distal helix binding, interactions with other potentially less favorable sites could occur and contribute to the bound regulatory domain (RD) conformational ensemble. Such a diverse ensemble of strongly and weakly bound conformations is increasingly evident in complexes involving intrinsically disordered peptides (IDPs) and globular targets^{27,69} and may be adopted by CaN, as well. It is also interesting that CD experiments described in ref 1 suggested that the distal helix contact is abolished at temperatures above 38 °C. It is tempting therefore to speculate that the comparatively larger RMSFs of the bound distal helix configurations relative to the CaMBR, in addition to the weaker interaction energies, may render the distal helix interaction susceptible to melting.

Strengthening the case for the involvement of the CaM site D in binding the CaN distal helix are our comparisons against two CaM variants with substantially impaired ability to relieve enzyme autoinhibition in another CaM target, MLCK.³⁷ CaM appears to relieve MLCK autoinhibition⁷⁰ through binding the kinase's regulatory domain⁷¹ and adopts a conformation similar to that of the CaN–CaM complex with CaM “wrapping” around an α -helical CaMBR motif (see also [Figure 8a](#)).^{1,68} Importantly, both appear to utilize secondary

interactions beyond the CaMBR motif, as was shown by Van Lierop et al.³⁷ for MLCK that K30E and G40D mutations far from its CaMBR-binding domain prevented CaM-dependent kinase activity. These sites are localized to the site D region we identified for distal helix binding in our study. Although the secondary interactions in MLCK likely involve CaM binding directly adjacent to the enzyme's catalytic domain,⁷² we speculated that mutagenesis of these CaM residues could also impact CaN activation but instead by disrupting distal helix interactions. We confirmed this hypothesis in our computational model by demonstrating less favorable distal helix binding scores and validated these predictions via a pNPP assay.

Assessment of Phosphatase Activity. To challenge our hypothesis that impaired distal helix binding to CaM reduce CaN activity, we used kinetic phosphatase assays with the substrate pNPP on WT and the aforementioned CaM mutants. The Michaelis constant, K_M , obtained from these experiments informs on the ability of the catalytic site to bind and dephosphorylate pNPP. This substrate is specific to the catalytic site due to its low molecular weight, which allows for a probe of the extent to which CaM binding removes the AID. Mutations in the distal helix region that disrupt its folding and allow the AID to bind to the catalytic site would result in reduced pNPP binding (higher K_M). This explanation has been used by earlier authors studying the inhibitory properties of the AID as a peptide.²⁸ We reported significantly higher K_M values for both K30E and G40D based on our pNPP assay, thus these mutants evidence weaker distal helix binding that impedes removal of the AID from the CaN catalytic site. As a result, the CaM variants reduce the CaN catalysis of the dephosphorylation reaction. This can be interpreted as the AID competing with pNPP at the catalytic site and yielding a reduced apparent substrate affinity. This loss of affinity coincides with 40% increases in K_M reported for CaN A454E relative to WT CaN,¹ which were attributed to impaired distal helix formation. In contrast, for common peptide-based dephosphorylation targets like RII²⁸ that bind to sites outside of the catalytic site (the LxVP site), binding, and hence K_M , would be unaffected by mutations in the distal helix region.

Tether Model of CaM-Dependent CaN Activation. We recognize that a shortcoming of our modeling approach is that it is limited to simulations of CaM complexes with fragments of the CaN regulatory domain, whereas distal helix binding's effects on CaN activity are coupled to the entire regulatory domain and, specifically, the AID. We therefore discuss a qualitative description of “linker” dynamics of the regulatory domain appropriate for the AID-dependent inactivation of CaN. Specifically, we speculate that we can describe extents of CaN inactivation based on the AID's effective concentration at the CaN catalytic site as determined by the formation of distal helix–CaM interactions. This effective concentration is controlled by the tethering of the AID to CaN, which effectively confines the AID to a smaller volume (compared to that of free diffusion) that results in a higher probability of interaction with the catalytic site.⁷³ We use this effective concentration perspective to qualitatively assess how distal helix interactions with CaM impact CaN activity, as explicit all-atom simulations of the complete regulatory domain (RD) are prohibitively expensive. Here we leveraged theoretical models of protein activation^{74,75} by describing binding of the AID to the CaN catalytic domain as an intra-PPI. This PPI leverages a

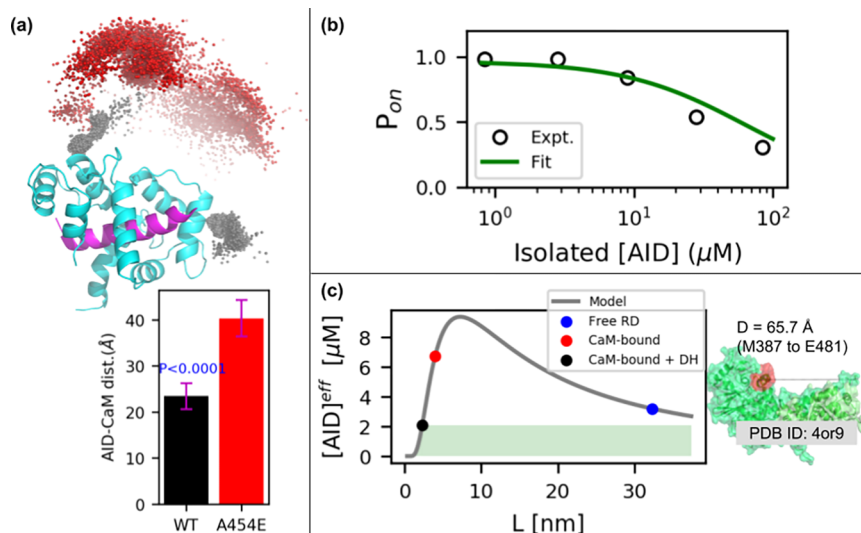


Figure 9. (a) Distribution of the AID center of mass (COM) relative to the CaM–CaMBR complex. The black and red spheres represent the COMs of AID in the WT and A454E cases, respectively. The bottom panel depicts the distance between COMs of AID and CaM. The *p* value above the WT bar is for the null hypothesis that the WT center of mass is the same as that of A454E. (b) Fitting of the competitive inhibitor model (eq 5) to experimental data from ref 76. (c) Effective AID concentrations calculated via eq 4. The shaded green area represents the [AID]^{eff} that leads to CaN's activation. The right panel illustrates the assumed distance between CaMBR and the catalytic site. The value is set as 66 Å in this study.

molecular tether (the regulatory domain) to enhance the local effective AID (*p*) concentration near the catalytic domain.

To illustrate this principle in CaN, we provide a basic extension of a linker-dependent modulation model we recently applied to the calcium-dependent troponin I (TnI) switch domain binding to troponin C (TnC).⁷³ For this reaction, binding of Ca²⁺ to TnC generates a conformation that can facilitate TnI binding:



hence, increasing the TnI concentration promotes the generation of TnC-TnI with fewer equivalents of Ca²⁺. In the tethered state, we estimated that the effective switch peptide concentration was an order of magnitude greater near its TnC target than would be expected for a 1:1 stoichiometric ratio of untethered (free) switch peptide to TnC. Accordingly, we experimentally confirmed that formation of the TnC/TnI switch peptide occurred at lower Ca²⁺ concentrations for the TnC-tethered TnI than for a cleaved system, in which both TnC and TnI were untethered.⁷³

In a similar vein, we created a hypothetical linker-based model of CaN activation, based on a polymer theory-based description for the probability distribution of the linker spanning the CaMBR and AID domains (see Figure 9). We introduce this model with several assumptions. First, we postulate the CaN inhibition is dependent on the free AID concentration, of which the latter is determined by the regulatory domain (RD) “tether” length. This tether length can assume three distributions associated with the CaM-free, CaMBR-bound CaM, and CaMBR- and distal helix-bound CaM. Lastly, for the sake of simplicity, we assume that the distal helix binds CaM independent of the AID’s bound state, though in reality we recognize there will be a competition between these two events.

Under these assumptions, we describe the effective AID concentration at the CaN catalytic domain, based on the regulatory domain (RD) linker length in its CaM-free,

CaMBR-bound CaM, and CaMBR- and distal helix-bound CaM states. We based this on an effective concentration model for tethered ligands suggested by Van Valen et al.⁷⁴

$$[\text{AID}]^{\text{eff}} = \left(\frac{3}{4\pi\xi L} \right)^{3/2} \exp\left(-\frac{3D^2}{4\xi L} \right) \quad (4)$$

where *D* is the distance between CaMBR and the catalytic site, *L* is the linker length, and ξ is the persistence length. The units of [AID]^{eff} in eq 4 were found via fitting to existing experimental data. Namely, we used experimental assays that investigated the competitive inhibitory effect of the isolated AID peptide on CaN phosphate activity on substrate peptide.^{76,77} In the assays, the decrease in phosphatase activity was recorded as the isolated AID peptide was added to intact CaN preincubated with CaM and the substrate RII peptide. According to the experimental setup, three competitive components could bind the catalytic site of CaN: substrate RII peptide, isolated AID peptide, and tethered AID from the intact CaN itself. Similar to the definition of *P*_{on} that represents the probability of switch peptide being on under the competitive binding of free ligand and tethered ligand to receptor in ref 74, we also defined a *P*_{on} that represents the percentage of CaN phosphate activity on the substrate RII peptide under competitive binding from the isolated AID peptide and tethered AID:

$$P_{\text{on}} = \frac{1 + \frac{[\text{RII}]}{K_{d1}}}{1 + \frac{[\text{RII}]}{K_{d1}} + \frac{[\text{AID}]}{K_{d2}} + \frac{[\text{tAID}]}{K_{d2}}} \quad (5)$$

where [RII], [AID], and [tAID] are concentrations of the substrate, isolated AID peptide, and tethered AID peptide, respectively. [RII] is set as 5 μM according to the experimental setup, and the dissociation constant of the substrate (*K*_{d1}) is assumed to be 10 μM. The tethered AID peptide is assumed to have the same dissociation constant as the isolated peptide with an experimentally estimated *K*_{d2} of 40 μM.^{76,77} The fitting

of eq 5 to experimental data in ref 76 with [tAID] as the free parameter is shown in Figure 9b. [tAID] was fitted as $2.07 \mu\text{M}$, and this value corresponds to the $[\text{AID}]^{\text{eff}}$ of the “CaMBR- and distal helix-bound CaM” case in our tether model. In the following tether model analysis, the $[\text{AID}]^{\text{eff}}$ from eq 4 was scaled by [tAID] to give meaningful units for the effective AID concentration.

We first provide a rough estimate for the linker length through simulations of residues E415–M490 C-terminal to the CaMBR (see Figure 9a). Starting from WT/A454E site D simulations, we fused an optimized fragment (residues K459–M490) containing AID built by TLEAP to the C-terminus of the distal helix in the representative structure of the first two most populated clusters. The complete structures were resolved and simulated for $\approx 0.7 \mu\text{s}$ as described in Section S1.1. These simulations indicate that the WT AID–CaM distance is approximately 23 \AA , versus approximately 40 \AA for the A454E variant that precludes distal helix binding.

On the basis of these data, in Figure 9c we demonstrate the effective AID concentration over a range of ligand lengths (L), predicted from eq 4 assuming $D = 66 \text{ \AA}$ for the distance between CaM and the CaN AID-binding site and $\xi = 3 \text{ \AA}$.⁷⁸ The black dot represents the CaMBR- and distal helix-bound case, which has a tethered ligand length estimated from our simulation of approximately 23 \AA or roughly eight free amino acids. The blue dot represents free RD, which has a ligand length of 95 residues (M387–E481). The red dot represents the CaMBR-bound (no distal helix interaction as for the A454E case; in this case, the tethered ligand length estimated from our simulation as 40 \AA). On the basis of these linker lengths, the corresponding $[\text{AID}]^{\text{eff}}$ values for CaMBR-bound (A454E) states were 6.76 and $2.07 \mu\text{M}$ for the CaMBR- and distal helix-bound case. For the free RD case, the $[\text{AID}]^{\text{eff}}$ is $3.20 \mu\text{M}$. In other words, the distal helix–CaM interaction decreases the AID effective concentration near the catalytic site relative to the free (no CaM) RD or CaMBR-only bound configurations. Hence, the binding of both the CaMBR and distal helix relieves CaN autoinhibition to the greatest extent. This approximate model is therefore consistent with the experimental trends in activity data reported in the literature,^{1,79} namely that maximal CaN activation requires CaM binding.

Limitations. We observed appreciable degrees of α -helical and β -sheet character in the regulatory domain that were not evident in the CD data from ref 14. A primary distinction between the modeling and experimental studies is that we used a regulatory domain fragment (residues A391–I458) that was much smaller than the full-length domain of Rumi-Masante et al.,¹⁴ owing to the computational expense. It is possible that there are different tendencies to form secondary structure, on the basis of the regulatory domain length. Because we simulated only a small fragment of the RD domain, this might have increased the peptide’s preference for α -helical structure than would otherwise be observed in measurements of the entire RD. For instance, it has been shown that IDPs have a length-dependent preference of residue compositions as a longer IDP has more enriched K, E, and P than a short IDP,⁸⁰ implying the conformational properties of IDPs that are determined by the sequence charge distribution⁶¹ are also length-dependent. As a concrete example, Lin et al.⁸¹ reported that the 40-residue disordered amyloid β -monomer has reduced β -hairpin propensity compared to that of the longer 42-residue monomer.

We additionally recognize that differences in ionic strength or solvent composition might influence the percentage of α -helical character, although this seemed to be a modest effect in our simulations of CaMBR alone.²⁷ Importantly, in that study, we reported negligible α -helical character for that isolated CaMBR peptide, which suggests that our force field was not artificially stabilizing α -helices, as had been an issue in earlier modeling studies of IDPs.^{82,83} Nevertheless, the potential overestimate of the α -helical content for the isolated peptide is probably of little consequence, because the predicted bound distal helix was shown to exhibit significant α -helical content consistent with experiment.

We utilized REMD to sample the distal helix sequence in the absence of CaM; although REMD has been shown to perform well in terms of qualitatively describing the conformational landscape, chemical shifts, and α -helix stability for peptides of lengths comparable to the distal helix,^{84–86} we did not have the means to experimentally validate the predicted apo ensembles. Nevertheless, the simulations provide testable hypotheses in terms of the α -helical content. We additionally limited ourselves to subsets of the CaM surface for the docking search, which represented approximately 38% of the solvent-exposed surface area. However, given that the microsecond-length simulations were sufficient to reorient the site B configurations into the D site, we anticipate the docked distal helix candidates reasonably sampled the thermodynamically accessible regions of the CaM surfaces. Although it has been demonstrated that binding of the RD to CaM is diffusion-limited, it is also possible that the intermediate complexes could be further optimized to form a final bound state, which would perhaps lead to more accurate assessments of critical intermolecular contacts and energy estimates. For the latter, alchemical methods such as thermodynamic integration may provide more accurate affinity estimates, albeit at a substantially greater computational expense compared to “end point” methods like MM-GBSA. In addition, more detailed simulations of the RD ensemble in the presence of the complete CaM and CaN structures are needed to more accurately characterize the effective AID distribution controlling CaN (in)activation.

Lastly, there are several considerations that could improve the accuracy of the tethering model in the Discussion. These include assumptions that the linker follows a random-walk chain distribution, that the catalytic domain does not attract and thereby bias the AID distribution, and that the CaN molecule does not sterically clash with the linker chain. In addition, precise knowledge of the CaM distribution relative to the CaN B chain would be needed to refine the effective linker lengths. Despite these assumptions, the model provides a qualitative basis for how regulatory domain (RD) mutations or variations in regulatory domain (RD) length could influence the efficiency of CaN (in)activation, similar to the model systems with synthetic linkers, as in ref 87.

Additional Considerations. There are several compelling directions to pursue that would provide essential clues governing CaM-dependent CaN activation. For one, we have predicted several contacts that appear to be involved in stabilizing the distal helix region; mutagenesis of these potential “hot spots” on CaM and measurements of subsequent CaN phosphatase activity could help validate this site. In addition, more detailed characterization of the RD intrinsically disordered conformation ensemble would benefit future modeling. Given the difficulty in probing ensemble

properties of IDPs, it is likely that modeling and experiment, such as fluorescence resonance energy transfer (FRET) labeling, should work in tandem toward this goal. Furthermore, relating these RD ensemble properties to the propensity for AID and CaN catalytic domain interactions would comprise an essential step toward a complete model of CaM-dependent CaN activation.

We anticipate that the findings of this study could broadly expand to other classes of CaM-dependent targets, namely enzymes that have autoinhibitory domains such as the CaM-dependent kinases (CaMKI and CaMKII) and MLCK.⁸⁸ Like CaN, these enzymes feature CaM-binding regions that are disordered in the absence of CaM.^{64,89} In contrast to CaN, the CaM-binding regions are nearly adjacent to their autoinhibitory domains.⁸⁸ As for CaN, the autoinhibitory domain and CaM-binding region are ~50 residues apart. For this reason, CaM essentially competes with the target for its regulatory domain, whereas for CaN, CaM binding essentially controls the spatial probability distribution of the AID by modulating the “tether length” of the regulatory domain. Despite this distinction, at least for MLCK, a secondary interaction between CaM and a region beyond CaMBR of MLCK might be necessary for the latter’s activation,³⁹ thus raising the possibility that other enzymes share similar CaM-dependent activation mechanisms as we report for CaN.

CONCLUSIONS

We have developed a computational strategy for elucidating potential binding poses for a secondary interaction (the “distal helix”) between the CaN regulatory domain and CaM that is apparently essential for competent CaN activation. We combined REMD simulations of isolated distal helix peptides, protein–protein docking of the distal helix peptides to the CaMBR-bound CaM surface, and microsecond-scale MD simulations of candidate poses to implicate a so-called CaM site D in binding the CaN distal helix. The predicted site D region is in part stabilized through direct interactions with K30 and indirectly through G40, which is consistent with experimental probes of a CaM-activated enzyme, MLCK. We confirmed the predictions via a pNPP phosphatase assay in which mutations K30E and G40D in CaM reduced CaN activity compared with that of WT CaM. With these data, we provide a qualitative model of AID-dependent CaN activation, which can be used to further refine potential molecular mechanisms governing the activation process and susceptibility to missense mutations. Importantly, our data suggest a potentially novel mechanism of CaM-dependent target regulation whereby interactions distal from the canonical CaM peptide-binding motif control target autoinhibition. Given the broad range of physiological processes mediated by binding of CaM to intrinsically disordered target proteins,⁶⁰ the mechanistic details of CaN activation in this study may extend to other CaM targets, including CaM-dependent channels and cytoskeletal components.^{60,90}

ASSOCIATED CONTENT

Supporting Information

The Supporting Information is available free of charge on the ACS Publications website at DOI: [10.1021/acs.biochem.9b00626](https://doi.org/10.1021/acs.biochem.9b00626).

Additional information regarding details of the method and supporting analysis ([PDF](#))

Accession Codes

Calmodulin (CaM), UniProtKB P0DP23; calcineurin (CaN), UniProtKB PPP3CA.

AUTHOR INFORMATION

Corresponding Author

*E-mail: pkekeneshuskey@luc.edu.

ORCID

Bin Sun: [0000-0003-2583-4493](https://orcid.org/0000-0003-2583-4493)

Trevor P. Creamer: [0000-0001-8868-8724](https://orcid.org/0000-0001-8868-8724)

Funding

Research reported in this publication was supported by the Maximizing Investigators’ Research Award (MIRA) (R35) from the National Institute of General Medical Sciences (NIGMS) of the National Institutes of Health (NIH) under Grant R35GM124977. This work was also supported by Grant R01HL138579.

Notes

The authors declare no competing financial interest.

ACKNOWLEDGMENTS

This work used the Extreme Science and Engineering Discovery Environment (XSEDE),⁹¹ which is supported by National Science Foundation under Grant ACI-1548562.

DEDICATION

The authors dedicate this study to the late Jeffry Madura, Ph.D., whose contributions to computational chemistry and the scientific community as a whole will be forever cherished.

REFERENCES

- (1) Dunlap, T. B., Cook, E. C., Rumi-Masante, J., Arvin, H. G., Lester, T. E., and Creamer, T. P. (2013) The distal helix in the regulatory domain of calcineurin is important for domain stability and enzyme function. *Biochemistry* 52, 8643–8651.
- (2) Rusnak, F., and Mertz, P. (2000) Calcineurin: Form and Function. *Physiol. Rev.* 80, 1483–1521.
- (3) Klee, C. B., Ren, H., and Wang, X. (1998) Regulation of the Calmodulin-stimulated Protein Phosphatase, Calcineurin. *J. Biol. Chem.* 273, 13367–13370.
- (4) Kissinger, C. R., et al. (1995) Crystal structures of human calcineurin and the human FKBP12–FK506–calcineurin complex. *Nature* 378, 641–644.
- (5) Griffith, J. P., Kim, J. L., Kim, E. E., Sintchak, M. D., Thomson, J. A., Fitzgibbon, M. J., Fleming, M. A., Caron, P. R., Hsiao, K., and Navia, M. A. (1995) X-ray structure of calcineurin inhibited by the immunophilin-immunosuppressant FKBP12–FKS06 complex. *Cell* 82, 507–522.
- (6) Li, H., Zhang, L., Rao, A., Harrison, S. C., and Hogan, P. G. (2007) Structure of Calcineurin in Complex with PVIVIT Peptide: Portrait of a Low-affinity Signalling Interaction. *J. Mol. Biol.* 369, 1296–1306.
- (7) Ye, Q., Wang, H., Zheng, J., Wei, Q., and Jia, Z. (2008) The complex structure of calmodulin bound to a calcineurin peptide. *Proteins: Struct., Funct., Genet.* 73, 19–27.
- (8) Jin, L., and Harrison, S. C. (2002) Crystal structure of human calcineurin complexed with cyclosporin A and human cyclophilin. *Proc. Natl. Acad. Sci. U. S. A.* 99, 13522–13526.
- (9) Sheftic, S. R., Page, R., and Peti, W. (2016) Investigating the human Calcineurin Interaction Network using the i LxVP SLiM. *Sci. Rep.* 6, 38920.
- (10) Takeuchi, K., Roehrl, M. H., Sun, Z. Y. J., and Wagner, G. (2007) Structure of the Calcineurin-NFAT Complex: Defining a T Cell Activation Switch Using Solution NMR and Crystal Coordinates. *Structure* 15, 587–597.

- (11) Ye, Q., Li, X., Wong, A., Wei, Q., and Jia, Z. (2006) Structure of Calmodulin Bound to a Calcineurin Peptide: A New Way of Making an Old Binding Mode. *Biochemistry* 45, 738–745.
- (12) Majava, V., and Kursula, P. (2009) Domain swapping and different oligomeric states for the complex between calmodulin and the calmodulin-binding domain of calcineurin A. *PLoS One* 4, e5402.
- (13) Manalan, A. S., and Klee, C. B. (1983) Activation of calcineurin by limited proteolysis. *Proc. Natl. Acad. Sci. U. S. A.* 80, 4291–4295.
- (14) Rumi-Masante, J., Rusinga, F. I., Lester, T. E., Dunlap, T. B., Williams, T. D., Dunker, A. K., Weis, D. D., and Creamer, T. P. (2012) Structural basis for activation of calcineurin by calmodulin. *J. Mol. Biol.* 415, 307–317.
- (15) Shen, X., Li, H., Ou, Y., Tao, W., Dong, A., Kong, J., Ji, C., and Yu, S. (2008) The Secondary Structure of Calcineurin Regulatory Region and Conformational Change Induced by Calcium/Calmodulin Binding. *J. Biol. Chem.* 283, 11407–11413.
- (16) Fruman, D. A., Klee, C. B., Bierer, B. E., and Burakoff, S. J. (1992) Calcineurin phosphatase activity in T lymphocytes is inhibited by FK 506 and cyclosporin A. *Proc. Natl. Acad. Sci. U. S. A.* 89, 3686–3690.
- (17) Parsons, J. N., Wiederrecht, G. J., Salowe, S., Burbaum, J. J., Rokosz, L. L., Kincaid, R. L., and O'Keefe, S. J. (1994) Regulation of calcineurin phosphatase activity and interaction with the FK-506??FK-506 binding protein complex. *J. Biol. Chem.* 269, 19610–19616.
- (18) Li, J., Jia, Z. G., Zhou, W. C., and Wei, Q. (2009) Calcineurin regulatory subunit B is a unique calcium sensor that regulates calcineurin in both calcium-dependent and calcium-independent manner. *Proteins: Struct., Funct., Genet.* 77, 612–623.
- (19) Harish, B. M., Saraswathi, R., Vinod, D., and Devaraju, K. S. (2016) Discovery of a latent calcineurin inhibitory peptide from its autoinhibitory domain by docking, dynamic simulation, and in vitro methods. *J. Biomol. Struct. Dyn.* 34, 983–992.
- (20) Rodríguez, A., Roy, J., Martínez-Martínez, S., López-Maderuelo, M. D., Niño-Moreno, P., Ortí, L., Pantoja-Uceda, D., Pineda-Lucena, A., Cyert, M. S., and Redondo, J. M. (2009) A Conserved Docking Surface on Calcineurin Mediates Interaction with Substrates and Immunosuppressants. *Mol. Cell* 33, 616–626.
- (21) Grigoriu, S., Bond, R., Cossio, P., Chen, J. A., Ly, N., Hummer, G., Page, R., Cyert, M. S., and Peti, W. (2013) The Molecular Mechanism of Substrate Engagement and Immunosuppressant Inhibition of Calcineurin. *PLoS Biol.* 11, e1001492.
- (22) Zhao, Y., Zhang, J., Shi, X., Li, J., Wang, R., Song, R., Wei, Q., Cai, H., and Luo, J. (2016) Quercetin targets the interaction of calcineurin with LxVP-type motifs in immunosuppression. *Biochimie* 127, 50–58.
- (23) Song, R., Li, J., Zhang, J., Wang, L., Tong, L., Wang, P., Yang, H., Wei, Q., Cai, H., and Luo, J. (2017) Peptides derived from transcription factor EB bind to calcineurin at a similar region as the NFAT-type motif. *Biochimie* 142, 158–167.
- (24) Nagulapalli, M., Parigi, G., Yuan, J., Gsponer, J., Deraos, G., Bamm, V. V., Harauz, G., Matsoukas, J., De Planque, M. R., Gerothanassis, I. P., Babu, M. M., Luchinat, C., and Tzakos, A. G. (2012) Recognition pliability is coupled to structural heterogeneity: A calmodulin intrinsically disordered binding region complex. *Structure* 20, 522–533.
- (25) Gsponer, J., Christodoulou, J., Cavalli, A., Bui, J. M., Richter, B., Dobson, C. M., and Vendruscolo, M. (2008) A Coupled Equilibrium Shift Mechanism in Calmodulin-Mediated Signal Transduction. *Structure* 16, 736–746.
- (26) Liu, F., Chu, X., Lu, H. P., and Wang, J. (2017) Molecular mechanism of multispecific recognition of Calmodulin through conformational changes. *Proc. Natl. Acad. Sci. U. S. A.* 114, E3927–E3934.
- (27) Sun, B., Cook, E. C., Creamer, T. P., and Kekenes-Huskey, P. M. (2018) Electrostatic control of calcineurin's intrinsically-disordered regulatory domain binding to calmodulin. *Biochim. Biophys. Acta, Gen. Subj.* 1862, 2651–2659.
- (28) Dunlap, T. B., Guo, H.-F., Cook, E. C., Holbrook, E., Rumi-Masante, J., Lester, T. E., Colbert, C. L., Vander Kooi, C. W., and Creamer, T. P. (2014) Stoichiometry of the Calcineurin Regulatory Domain–Calmodulin Complex. *Biochemistry* 53, 5779–5790.
- (29) Nevola, L., and Giralt, E. (2015) Modulating protein–protein interactions: the potential of peptides. *Chem. Commun.* 51, 3302–3315.
- (30) Jochim, A. L., and Arora, P. S. (2009) Assessment of helical interfaces in protein–protein interactions. *Mol. BioSyst.* 5, 924–926.
- (31) Bullock, B. N., Jochim, A. L., and Arora, P. S. (2011) Assessing helical protein interfaces for inhibitor design. *J. Am. Chem. Soc.* 133, 14220–14223.
- (32) Pierce, B. G., Wiehe, K., Hwang, H., Kim, B.-H., Vreven, T., and Weng, Z. (2014) ZDOCK server: interactive docking prediction of protein–protein complexes and symmetric trimers. *Bioinformatics* 30, 1771–1773.
- (33) Chaudhury, S., Berroondo, M., Weitzner, B. D., Muthu, P., Bergman, H., and Gray, J. J. (2011) Benchmarking and analysis of protein docking performance in Rosetta v3.2. *PLoS One* 6, e22477.
- (34) Hu, X., Lee, M. S., and Wallqvist, A. (2009) Interaction of the disordered Yersinia effector protein YopE with its cognate chaperone SycE. *Biochemistry* 48, 11158–11160.
- (35) Schiffer, J. M., Malmstrom, R. D., Parnell, J., Ramirez-Sarmiento, C., Reyes, J., Amaro, R. E., and Komives, E. A. (2016) Model of the Ankyrin and SOCS Box Protein, ASB9, E3 Ligase Reveals a Mechanism for Dynamic Ubiquitin Transfer. *Structure* 24, 1248–1256.
- (36) Bui, J. M., and Gsponer, J. (2014) Phosphorylation of an intrinsically disordered segment in Ets1 shifts conformational sampling toward binding-competent substates. *Structure* 22, 1196–1203.
- (37) Van Lierop, J. E., Wilson, D. P., Davis, J. P., Tikunova, S., Sutherland, C., Walsh, M. P., and Johnson, J. D. (2002) Activation of smooth muscle myosin light chain kinase by calmodulin. Role of LY30 and GLY40. *J. Biol. Chem.* 277, 6550–6558.
- (38) Zhi, G., Abdullah, S. M., and Stull, J. T. (1998) Regulatory segments of Ca²⁺/calmodulin-dependent protein kinases. *J. Biol. Chem.* 273, 8951–8957.
- (39) Soderling, T. R., and Stull, J. T. (2001) Structure and regulation of calcium/calmodulin-dependent protein kinases. *Chem. Rev.* 101, 2341–2351.
- (40) Case, D., et al. (2016) *Amber 16*, University of California, San Francisco.
- (41) Lindorff-Larsen, K., Piana, S., Palmo, K., Maragakis, P., Klepeis, J. L., Dror, R. O., and Shaw, D. E. (2010) Improved side-chain torsion potentials for the Amber ff99SB protein force field. *Proteins: Struct., Funct., Genet.* 78, 1950–1958.
- (42) Case, D. A., Cheatham, T. E., Darden, T., Gohlke, H., Luo, R., Merz, K. M., Onufriev, A., Simmerling, C., Wang, B., and Woods, R. J. (2005) The Amber biomolecular simulation programs. *J. Comput. Chem.* 26, 1668–1688.
- (43) Hawkins, G. D., Cramer, C. J., and Truhlar, D. G. (1996) Parametrized Models of Aqueous Free Energies of Solvation Based on Pairwise Descreening of Solute Atomic Charges from a Dielectric Medium. *J. Phys. Chem.* 100, 19824–19839.
- (44) Patriksson, A., and van der Spoel, D. (2008) A temperature predictor for parallel tempering simulations. *Phys. Chem. Chem. Phys.* 10, 2073–2077.
- (45) Zhang, W., Wu, C., and Duan, Y. (2005) Convergence of replica exchange molecular dynamics. *J. Chem. Phys.* 123, 154105.
- (46) Patel, S., Vierling, E., and Tama, F. (2014) Replica exchange molecular dynamics simulations provide insight into substrate recognition by small heat shock proteins. *Biophys. J.* 106, 2644–2655.
- (47) Ryckaert, J.-P., Cicotti, G., and Berendsen, H. J. (1977) Numerical integration of the cartesian equations of motion of a system with constraints: molecular dynamics of n-alkanes. *J. Comput. Phys.* 23, 327–341.
- (48) Mintseris, J., Pierce, B., Wiehe, K., Anderson, R., Chen, R., and Weng, Z. (2007) Integrating statistical pair potentials into protein complex prediction. *Proteins: Struct., Funct., Genet.* 69, 511–520.

- (49) Chen, R., and Weng, Z. (2002) Docking unbound proteins using shape complementarity, desolvation, and electrostatics. *Proteins: Struct., Funct., Genet.* 47, 281–294.
- (50) Jorgensen, W. L., Chandrasekhar, J., Madura, J. D., Impey, R. W., and Klein, M. L. (1983) Comparison of simple potential functions for simulating liquid water. *J. Chem. Phys.* 79, 926–935.
- (51) Maier, J. A., Martinez, C., Kasavajhala, K., Wickstrom, L., Hauser, K. E., and Simmerling, C. (2015) ff14SB: Improving the Accuracy of Protein Side Chain and Backbone Parameters from ff99SB. *J. Chem. Theory Comput.* 11, 3696–3713.
- (52) Berendsen, H. J. C., Postma, J. P. M., van Gunsteren, W. F., DiNola, A., and Haak, J. R. (1984) Molecular dynamics with coupling to an external bath. *J. Chem. Phys.* 81, 3684–3690.
- (53) Malmstrom, R. D., Lee, C. T., Van Wart, A. T., and Amaro, R. E. (2014) Application of Molecular-Dynamics Based Markov State Models to Functional Proteins. *J. Chem. Theory Comput.* 10, 2648–2657.
- (54) Genheden, S., and Ryde, U. (2015) The MM/PBSA and MM/GBSA methods to estimate ligand-binding affinities. *Expert Opin. Drug Discovery* 10, 449–461.
- (55) Immadisetty, K., and Madura, J. (2013) A review of monoamine transporter-ligand interactions. *Curr. Comput.-Aided Drug Des.* 9, 556–568.
- (56) Roe, D. R., and Cheatham, T. E. (2013) PTraj and CPPPTraj: Software for Processing and Analysis of Molecular Dynamics Trajectory Data. *J. Chem. Theory Comput.* 9, 3084–3095.
- (57) Kabsch, W., and Sander, C. (1983) Dictionary of protein secondary structure: Pattern recognition of hydrogen bonded and geometrical features. *Biopolymers* 22, 2577–2637.
- (58) Fiorin, G., Klein, M. L., and Hénin, J. (2013) Using collective variables to drive molecular dynamics simulations. *Mol. Phys.* 111, 3345–3362.
- (59) Cho, M. J., Vaghy, P. L., Kondo, R., Lee, S. H., Davis, J. P., Rehl, R., Heo, W. D., and Johnson, J. D. (1998) Reciprocal regulation of mammalian nitric oxide synthase and calcineurin by plant calmodulin isoforms. *Biochemistry* 37, 15593–15597.
- (60) Kursula, P. (2014) The many structural faces of calmodulin: A multitasking molecular jackknife. *Amino Acids* 46, 2295–2304.
- (61) Das, R. K., and Pappu, R. V. (2013) Conformations of intrinsically disordered proteins are influenced by linear sequence distributions of oppositely charged residues. *Proc. Natl. Acad. Sci. U. S. A.* 110, 13392–13397.
- (62) Guharoy, M., and Chakrabarti, P. (2007) Secondary structure based analysis and classification of biological interfaces: Identification of binding motifs in protein-protein interactions. *Bioinformatics* 23, 1909–1918.
- (63) Marques, M. A., Parvatiyar, M. S., Yang, W., de Oliveira, G., and Pinto, J. R. (2019) The missing links within troponin. *Arch. Biochem. Biophys.* 663, 95–100.
- (64) Dunlap, T. B., Kirk, J. M., Pena, E. A., Yoder, M. S., and Creamer, T. P. (2013) Thermodynamics of binding by calmodulin correlates with target peptide α -helical propensity. *Proteins: Struct., Funct., Genet.* 81, 607–612.
- (65) Zamoon, J., Nitu, F., Karim, C., Thomas, D. D., and Veglia, G. (2005) Mapping the interaction surface of a membrane protein: unveiling the conformational switch of phospholamban in calcium pump regulation. *Proc. Natl. Acad. Sci. U. S. A.* 102, 4747.
- (66) Zhou, G., Pantelopoulos, G. A., Mukherjee, S., and Voelz, V. A. (2017) Bridging Microscopic and Macroscopic Mechanisms of p53-MDM2 Binding with Kinetic Network Models. *Biophys. J.* 113, 785–793.
- (67) Paul, F., Noé, F., and Weikl, T. R. (2018) Identifying Conformational-Selection and Induced-Fit Aspects in the Binding-Induced Folding of PMI from Markov State Modeling of Atomistic Simulations. *J. Phys. Chem. B* 122, 5649–5656.
- (68) Grishaev, A., Anthis, N. J., and Clore, G. M. (2012) Contrast-matched small-angle x-ray scattering from a heavy-atom-labeled protein in structure determination: Application to a lead-substituted calmodulin-peptide complex. *J. Am. Chem. Soc.* 134, 14686–14689.
- (69) Dogan, J., Gianni, S., and Jemth, P. (2014) The binding mechanisms of intrinsically disordered proteins. *Phys. Chem. Chem. Phys.* 16, 6323–6331.
- (70) Hoeflich, K. P., and Ikura, M. (2002) Calmodulin in Action. *Cell* 108, 739–742.
- (71) Blumenthal, D. K., Takio, K., Edelman, A. M., Charbonneau, H., Titani, K., Walsh, K. A., and Krebs, E. G. (1985) Identification of the calmodulin-binding domain of skeletal muscle myosin light chain kinase. *Proc. Natl. Acad. Sci. U. S. A.* 82, 3187–3191.
- (72) Fitzsimons, D. P., Herring, B. P., Stull, J. T., and Gallagher, P. J. (1992) Identification of basic residues involved in activation and calmodulin binding of rabbit smooth muscle myosin light chain kinase. *J. Biol. Chem.* 267, 23903–23909.
- (73) Siddiqui, J. K., Tikunova, S. B., Walton, S. D., Liu, B., Meyer, M., de Tombe, P. P., Neilson, N., Kekenes-Huskey, P. M., Salhi, H. E., Janssen, P. M., Biesiadecki, B. J., and Davis, J. P. (2016) Myofilament Calcium Sensitivity: Consequences of the effective concentration of troponin I. *Front. Physiol.* 7, 632.
- (74) Van Valen, D., Haataja, M., and Phillips, R. (2009) Biochemistry on a Leash: The Roles of Tether Length and Geometry in Signal Integration Proteins. *Biophys. J.* 96, 1275–1292.
- (75) Shoemaker, B. A., Portman, J. J., and Wolynes, P. G. (2000) Speeding molecular recognition by using the folding funnel: the fly-casting mechanism. *Proc. Natl. Acad. Sci. U. S. A.* 97, 8868.
- (76) Fruman, D. A., Pai, S. Y., Burakoff, S. J., and Bierer, B. E. (1995) Characterization of a mutant calcineurin A alpha gene expressed by EL4 lymphoma cells. *Mol. Cell. Biol.* 15, 3857–3863.
- (77) Sagoo, J. K., Fruman, D. A., Wesselborg, S., Walsh, C. T., and Bierer, B. E. (1996) Competitive inhibition of calcineurin phosphatase activity by its autoinhibitory domain. *Biochem. J.* 320 (Part 3), 879–884.
- (78) Borcherds, W., Becker, A., Chen, L., Chen, J., Chemes, L. B., and Daughdrill, G. W. (2017) Optimal Affinity Enhancement by a Conserved Flexible Linker Controls p53 Mimicry in MdmX. *Biophys. J.* 112, 2038–2042.
- (79) Stemmer, P. M., and Klee, C. B. (1994) Dual Calcium Ion Regulation of Calcineurin by Calmodulin and Calcineurin B. *Biochemistry* 33, 6859–6866.
- (80) Peng, K., Radivojac, P., Vucetic, S., Dunker, A. K., and Obradovic, Z. (2006) Length-dependent prediction of protein in intrinsic disorder. *BMC Bioinf.* 7, 208.
- (81) Lin, Y. S., Bowman, G. R., Beauchamp, K. A., and Pande, V. S. (2012) Investigating how peptide length and a pathogenic mutation modify the structural ensemble of amyloid beta monomer. *Biophys. J.* 102, 315–324.
- (82) Fluit, A. M., and De Pablo, J. J. (2015) An Analysis of Biomolecular Force Fields for Simulations of Polyglutamine in Solution. *Biophys. J.* 109, 1009–1018.
- (83) Henriques, J., Cragnell, C., and Skepö, M. (2015) Molecular Dynamics Simulations of Intrinsically Disordered Proteins: Force Field Evaluation and Comparison with Experiment. *J. Chem. Theory Comput.* 11, 3420–3431.
- (84) Guo, Z., Mohanty, U., Noehre, J., Sawyer, T. K., Sherman, W., and Krilov, G. (2010) Probing the α -helical structural stability of stapled p53 peptides: Molecular dynamics simulations and analysis: Research article. *Chem. Biol. Drug Des.* 75, 348–359.
- (85) Miller, Y., Ma, B., and Nussinov, R. (2010) Zinc ions promote Alzheimer A aggregation via population shift of polymorphic states. *Proc. Natl. Acad. Sci. U. S. A.* 107, 9490–9495.
- (86) Best, R. B., and Mittal, J. (2011) Free-energy landscape of the GB1 hairpin in all-atom explicit solvent simulations with different force fields: Similarities and differences. *Proteins: Struct., Funct., Genet.* 79, 1318–1328.
- (87) Qin, Y., Liu, J., Li, X., and Wei, Q. (2005) Preparation and characterization of a single-chain calcineurin-calmodulin complex. *Biochim. Biophys. Acta, Proteins Proteomics* 1747, 171–178.
- (88) Swulius, M. T., and Waxham, M. N. (2008) Ca²⁺/calmodulin-dependent protein kinases. *Cell. Mol. Life Sci.* 65, 2637–2657.

- (89) Myers, J. B., Zaegel, V., Coultrap, S. J., Miller, A. P., Bayer, K. U., and Reichow, S. L. (2017) The CaMKII holoenzyme structure in activation-competent conformations. *Nat. Commun.* **8**, 15742.
- (90) Zhang, M., Pascal, J. M., and Zhang, J.-F. (2013) Unstructured to structured transition of an intrinsically disordered protein peptide in coupling Ca²⁺-sensing and SK channel activation. *Proc. Natl. Acad. Sci. U. S. A.* **110**, 4828–4833.
- (91) Towns, J., Cockerill, T., Dahan, M., Foster, I., Gaither, K., Grimshaw, A., Hazlewood, V., Lathrop, S., Lifka, D., Peterson, G. D., Roskies, R., Scott, J. R., and Wilkins-Diehr, N. (2014) XSEDE: Accelerating Scientific Discovery. *Comput. Sci. Eng.* **16**, 62–74.